

High-Density Periodically Ordered Magnetic Cobalt Ferrite Nanodot Arrays by Template-Assisted Pulsed Laser Deposition

By Xingsen Gao,* Lifeng Liu, Balaji Birajdar, Michael Ziese, Woo Lee, Marin Alexe, and Dietrich Hesse

A novel nanopatterning method using pulsed laser deposition through an ultrathin anodic aluminium oxide (AAO) membrane mask is proposed to synthesize well-ordered nanodot arrays of magnetic CoFe_2O_4 that feature a wide range of applications like sensors, drug delivery, and data storage. This technique allows the adjustment of the array dimension from ~ 35 to ~ 300 nm in diameter and ~ 65 to ~ 500 nm in inter-dot distance. The dot density can be as high as 0.21 Terabit in^{-2} . The microstructure of the nanodots is characterized by SEM, TEM, and XRD and their magnetic properties are confirmed by well-defined magnetic force microscopy contrasts and by hysteresis loops recorded by a superconducting quantum interference device. Moreover, the high stability of the AAO mask enables the epitaxial growth of nanodots at a temperature as high as 550 °C. The epitaxial dots demonstrate unique complex magnetic domains such as bubble and stripe domains, which are switchable by external magnetic fields. This patterning method creates opportunities for studying novel physics in oxide nanomagnets and may find applications in spintronic devices.

1. Introduction

The hard ferrite spinel CoFe_2O_4 (CFO) has been intensively investigated for its large magnetocrystalline anisotropy and magnetostriction, chemical stability, and unique nonlinear spin-wave properties, as well as for its application potentials in spintronic devices, for example, magnetic sensors or memories.^[1–4] It has also been considered as a main component for multiferroic multilayers and composites.^[5] Nanometer-size CFO structures have also been one of the most frequently chosen systems for studying nanomagnetism. They show high potential for some important applications, ranging from data storage, sensors, and

drug delivery to bimolecular tagging, imaging, sensing, and separations.^[6–10] Up until now, a large variety of nanostructures like monodisperse particles,^[7,11] wires,^[12] curved bowls,^[13] and hollow spheres^[14] have been fabricated, and they demonstrate several unique structure–property relationships.^[15–18] All these state-of-the-art investigations are paving the way from basic research to industry applications.

For spintronic devices, a fundamentally essential step is to fabricate ordered arrays of nanomagnets on appropriate substrates, as required by the emerging information technologies such as ultrahigh density storage devices, sensors, magnetic random access memory devices, and logic devices.^[19,20] Although an increased interest exists in metal-based patterned magnets driven by modern lithography techniques in recent years, there are still only a few reports on patterned oxide magnets, probably due to their refractory and chemical inertness and

the lack of a suitable fabrication process for high-density and large-area nanodot arrays.

In this work, a combined top-down and bottom-up patterning technique involving pulsed laser deposition (PLD) and ultrathin nanoporous anodic aluminum oxide (AAO) membranes as stencil masks was employed to fabricate large-area nanosized CFO dot arrays. The AAO-based method is a unique approach for the direct growth of nanostructures at relatively high temperatures (up to 550 °C), enabling a high degree of control of the crystalline quality.^[21,22] The lift-off process can be solvent-free, thus avoiding cross-contamination during nanopatterning. We successfully fabricated well-ordered CFO arrays with diameters of nanodots ranging from 35 to 300 nm and an area density near 0.21 Terabits in^{-2} . Moreover, we have been able to achieve epitaxial nanodot structures by carefully adjusting the deposition parameters.

2. Results and Discussion

2.1. Microstructures of CFO Nanodot Arrays

The nanodot array is fabricated based on PLD through an ultrathin AAO template mask, as schematically illustrated in the flow chart of Figure 1a. A conducting layer of SrRuO_3 (SRO) was deposited,

[*] Dr. X.-S. Gao, Dr. L.-F. Liu, Dr. B. Birajdar, Dr. M. Alexe, Prof. D. Hesse
Max Planck Institute of Microstructure Physics
Weinberg 2, D-06120 Halle (Saale) (Germany)
E-mail: xgao@mpi-halle.de

Dr. M. Ziese
Div. of Superconductivity and Magnetism
University of Leipzig
D-04103 Leipzig (Germany)

Dr. W. Lee
Korea Research Institute of Standards and Science (KRISS)
Yuseong, 305-340 Daejeon (Korea)

DOI: 10.1002/adfm.200900422

then the AAO mask was transferred, followed by depositions of CFO using PLD. Finally the mask was removed and the ordered nanodot array was obtained. A representative atomic force microscopy (AFM) image of the resulting sample nanodot array is also shown in Figure 1b, which exhibits a well-ordered hexagonal arrangement of nanodots with an average diameter of ~ 50 nm and an interdot distance of ~ 104 nm.

Figure 2 shows scanning electron microscopy (SEM) images of nanodot arrays in different states of preparation, beginning with a SrTiO₃ (STO)/SRO substrate covered with an AAO mask. Figure 2a shows the AAO mask before deposition, which includes periodically ordered circularly shaped holes. Throughout this work we used self-organized AAO. Perfectly ordered AAO membranes and long-range ordered nanodot arrays could also be fabricated by imprint and other methods.^[21,23,24] The CFO was then deposited on the above substrates at a temperature of 450 °C and a vacuum of about 10^{-5} mbar to ensure that the CFO material properly reaches the substrate. Figure 2b shows the nanodot array after partially removing the AAO mask in order to visualize both CFO dots and mask. After lift-off, a well-ordered array of the CFO nanodots remains on the substrate (Fig. 2c). To get an insight into the degree of ordering, size distribution, and pair distribution function, nanodot arrays were analyzed using SEM (Fig. 2d). The nanodot array shows a sharp distribution in diameter that follows a Gaussian distribution function centered at 45 nm with a standard deviation of 5 nm. The pair distribution of the dots shows an apparently ordered correlation on a range of more than 1 μm and the nearest neighbor peak, which corresponds to the inter-dot period, is centered around 96 nm. In an area of $1 \times 1 \mu\text{m}^2$, fast Fourier transform (FFT) shows a nearly hexagonal structure similar to the typical honeycomb pattern of the AAO mask. Although a perfectly ordered structure can only be achieved in a range of a few micrometers using this technique, the mask has proven to be capable of further improvements. If combined with an imprint technique, long-range-ordered pores can be achieved on a wafer scale,^[25] enabling the application of this method in spintronic devices.

Cross-section images of nanodots and of a detached AAO mask were investigated by transmission electron microscopy (TEM), as shown in Figure 3. Well-defined CFO periodical dots were identified

with a sharp interface with the SRO layer (Fig. 3a). The average dot height was around 50 nm. Part of the AAO mask, detached from the substrate, is also visible in the figure. The composition of the CFO dots was qualitatively confirmed by energy-dispersive X-ray spectroscopy (EDX), in which Co and Fe can be easily identified in addition to Sr, Ru, and Ti from the substrate and electrode layer (Fig. 3b). The crystallinity was also studied by high-resolution TEM (HRTEM) as shown in Figure 3c, in which more than one crystallite can be indentified. This is also shown by the FFT of the HRTEM image (insert). The crystal lattice shows well-established CFO planes as illustrated in the magnified image (Fig. 3d). Although the entire dot is not a single crystal, the high stability of the mask allows further optimization of the deposition parameters, that is, temperature and ambient pressure, making the fabrication of high-quality epitaxial dots possible.

Using the described method, we were able to fabricate dots with tunable sizes simply by varying the size and inter-pore distance of the AAO mask. As illustrated in the AFM and SEM images in Figure 4, nanodot arrays with diameters ranging from 35 to 300 nm and inter-dot distances from 60 to 500 nm were achieved. The dot height can be varied in the range from a few up to a hundred nanometers by carefully controlling the deposition rate and duration. If we consider a single dot as one functional unit for potential devices (e.g., data storage), the memory density can reach as high as near 0.2 Terabits in.⁻² based on the calculation for a hexagonal array with an inter-dot distance of 60 nm.^[21]

2.2. Magnetic Properties

The magnetic properties of the nanodot array were characterized macroscopically by superconducting quantum interference device (SQUID) measurements and locally by magnetic force microscopy (MFM). Figure 5 shows both AFM topography and MFM micrographs for nanodot arrays with two different dot sizes (with an average diameter of ~ 60 nm for the small dots and ~ 300 nm for the larger dots). For the array with the smaller dots (Fig. 5a), the topography image shows a rather regular array structure and the corresponding MFM signal can be easily identified. Well-established bright–dark domain images were found and the contrast was very different from the surface topography, precluding any topography effects on the magnetic signals. The magnetic dots form dark–bright clusters each contained a number of dots with the same magnetic orientation. The formation of these clusters indicates the existence of dipole–dipole interactions between the magnetic dots. For the arrays of larger dots (Fig. 5c and d), an MFM dark–bright contrast is visible for each dot. These arrays show a more-or-less individual magnetic behavior of the dots. This implies that the dipole–dipole interaction between the large dots is relatively weak and not strong enough to overcome the barrier for magnetization reorientation. The magnetization of the large dots can be switched to form a uniform out-of-plane magnetization by applying an external magnetic field perpendicular to the surface, which is not the case for the small dots. As shown in Figure 5e and f, after applying and removing an out-of plane magnetic field to saturate the CFO nanodots, the remanent states of the dots demonstrate uniform single-domain bright contrast, while they turn to dark contrast if subjected to a reversed field, indicating a reversible switching of magnetization. It is worth

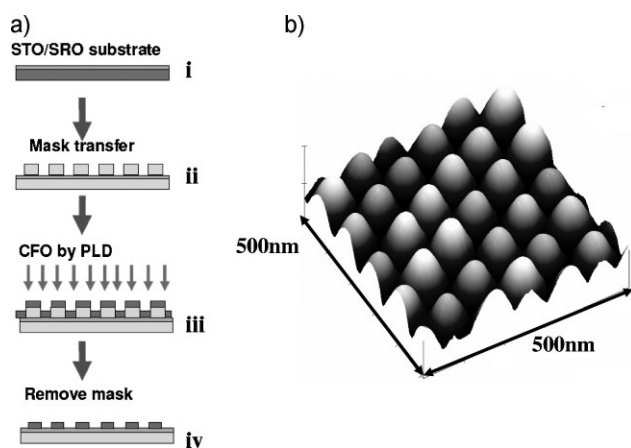


Figure 1. Schematic flow chart for the nanodot array fabrication procedure (a) and AFM image of an as-deposited CFO nanodot array (b).

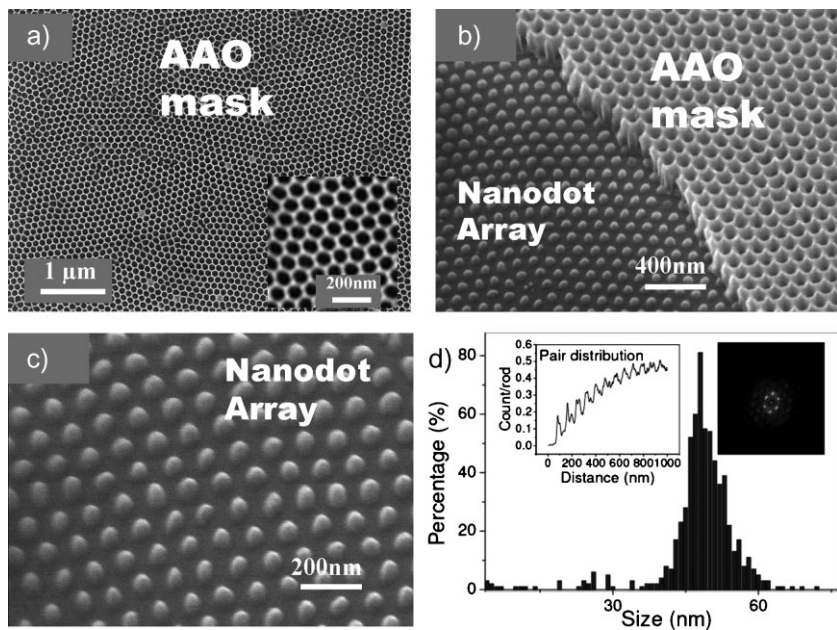


Figure 2. a) AAO mask on SRO/STO substrate. Inset: magnified image showing the ordered pores. b) CFO nanodot array together with a partially removed AAO mask. The image was obtained by tilting the sample by 45° in order to visualize the cross-section of the mask. c) Well-ordered CFO nanodot array. d) Size distribution of the CFO dots. Insets: Pair distribution function (PDF, left inset) and FFT (right inset) derived from the SEM image of a dot array showing the nearly hexagonally ordered structure.

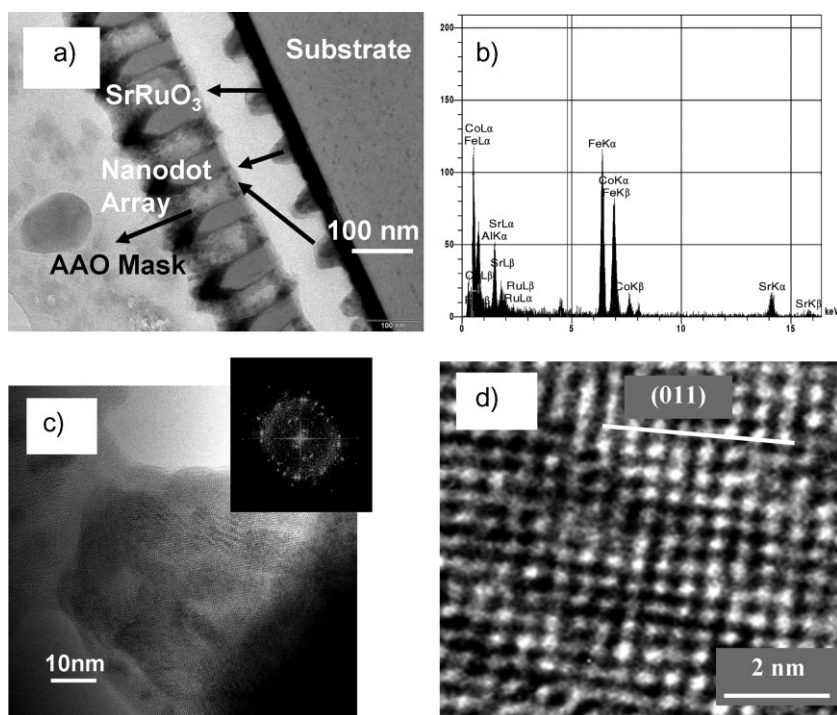


Figure 3. Cross-section TEM images of CFO dots. a) CFO dot array along with the detached AAO mask. b) EDX spectrum for a dot on a substrate to show its elemental composition. c) HRTEM of a CFO dot. Insets are the FFT pattern. d) Magnified high-resolution lattice image from (c).

mentioning that in-plane magnetization may also exist in the dots and contribute to the MFM contrast, but its interaction with the tip would be much weaker compared to the out-of-plane component. The observed dark–bright contrasts in MFM images are most likely from an out-of-plane component of magnetization at remanent state, which is switchable by a perpendicular magnetic field.

Figure 6 shows magnetic loops taken by SQUID along both in- and out-of-plane directions from a dot array with a dot diameter of 50 nm, an interdot distance of 104 nm, and a height of 40 nm. In both directions, relatively slim loops can be observed, indicating that the dots are soft magnets in nature. The out-of-plane loop shows a smaller remanent magnetization than that of the in-plane loop, implying a slightly in-plane easy axis. From the inserted enlarged loops, the in-plane coercive field can be determined as around ~170 Oe, which is much smaller than that of an epitaxial CFO film on a SRO/STO substrate (~3 000 Oe).^[26] In epitaxial CFO films, the large coercivity can be ascribed to magnetostrictive, magnetocrystalline, and shape anisotropies, among which the magnetostrictive anisotropy from clamping strain is the dominating factor.^[3,26] In our CFO islands, the magnetostrictive anisotropy can be greatly reduced by fast relaxation of the strain from the island edges, while the shape anisotropy and crystalline anisotropy can be released by forming noncontinuous islands and polycrystallites, respectively. Although the dipole–dipole interactions among dots add to the anisotropy, they are too weak compared to the internal anisotropy. As a result, the nanodot exhibits a more-or-less soft magnetic behavior, similar to an unstrained, bulk CFO single crystal, which displays a cubic-like crystalline anisotropy and slim loops in both in-plane and perpendicular orientations.^[27]

2.3. Epitaxial CFO Nanodot Array and Complex Magnetic Domains

For CFO nanodots, it is a challenging, although meaningful, task to directly deposit large-area epitaxial structures, which to the best of our knowledge has not been reported so far. By optimizing the deposition parameters, we were able to achieve an epitaxial nanodot array directly from deposition. Taking advantage of the large area (10 × 10 cm²) fabrication potential, we were able to fabricate and characterize the structure by X-ray diffraction (XRD). Figure 7a shows the XRD pattern for the nanodot array. The CFO (004) and (008) peaks

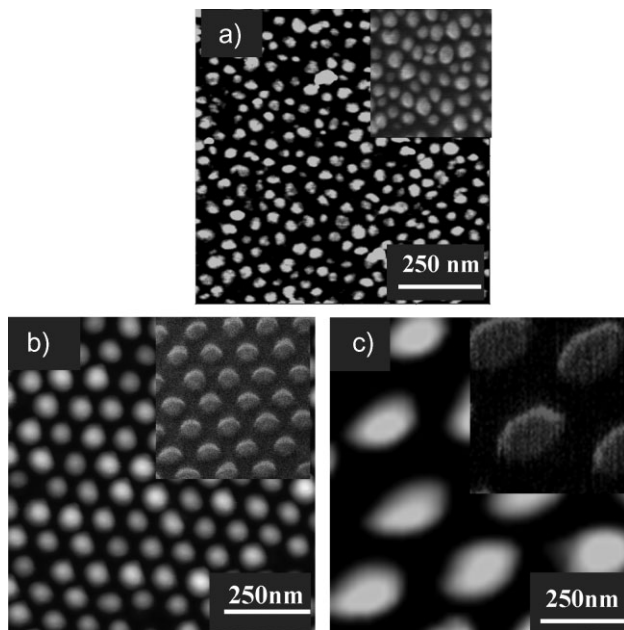


Figure 4. AFM images and corresponding SEM images (insets) for CFO dot arrays with various sizes. The average dot size and inter-dot period are a) ~ 35 and ~ 58 nm, b) ~ 58 and ~ 105 nm, and c) ~ 210 and ~ 450 nm, respectively.

can be identified although the peak intensity is rather weak. The epitaxial relation was confirmed by a Φ -scan (Fig. 7c), which shows four sharp peaks, indicating a cubic-on-cubic epitaxial growth of CFO on STO. The (004) rocking curve (Fig. 7b) shows a narrow full-width-at-half-maximum (FWHM) of 0.3° , indicating a good epitaxial quality. The epitaxial state could further be confirmed by the reciprocal space mapping along the STO(002) plane, in which the CFO(004) diffraction spot can be identified in spite of its weak intensity, further confirming its high-quality epitaxial nature (Fig. 7d). The CFO diffraction spot shows a more-or-less symmetric shape and is centered at $q = 0$, suggesting a good cubic-on-cubic epitaxial growth for the film on the substrate plane without a detectable tilting.

The magnetization of the CFO nanodots was further studied by MFM micrographs, as shown in Figure 8. To obtain the remanent states of the CFO dots (diameter: ~ 290 nm, height: ~ 80 nm), we premagnetized the nanodots by a field perpendicular to the substrate surface before imaging the MFM micrographs, and then a reversed field was applied to further examine the switching of the magnetic states. As shown in Figure 8b, the MFM micrographs of the dots after the initial magnetization do not show uniform single-domain states like the ones in Figure 5f, but rather exhibit a dark-bright contrast inside the dots, indicating a multidomain structure. As the area of the dark region is larger than that of the bright region for most dots, a net magnetization can be expected. After applying a reversed field (Fig. 8d), the dark-bright contrasts have changed, but the dots still have a complex domain structure.

To further understand the magnetic states, the MFM micrographs of some typical domain states were recorded and are shown in Figure 8e. Based on the contrast of the MFM images, we could identify the spin configurations for the dots (considering only the

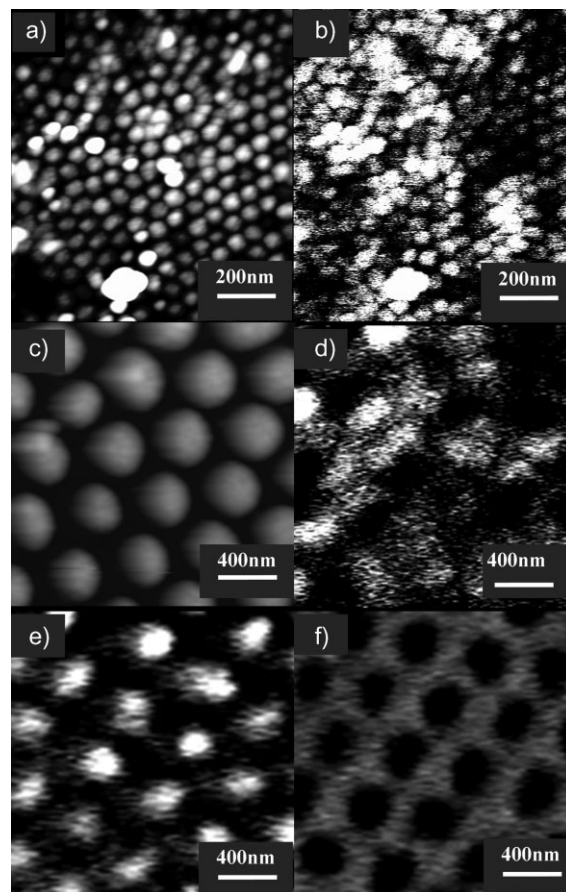


Figure 5. AFM topography images (a,c) and corresponding MFM micrographs (b,d) for the CFO nanodot arrays with different average nanodot diameters of ~ 60 nm (a,b) and ~ 300 nm (c,d). MFM images for the nanodot array shown in (c), pre-magnetized by a field (H) along the direction perpendicular to the surface (e) and by a reversed field ($-H$) along the opposite direction (f).

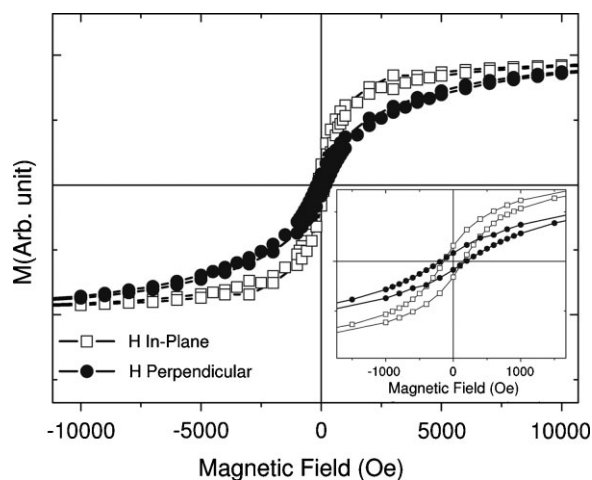


Figure 6. Hysteresis loops for the CFO nanodot array with an average dot diameter of ~ 50 nm and dot height of ~ 40 nm measured by SQUID at room temperature and at magnetic field along both in-plane and perpendicular directions.

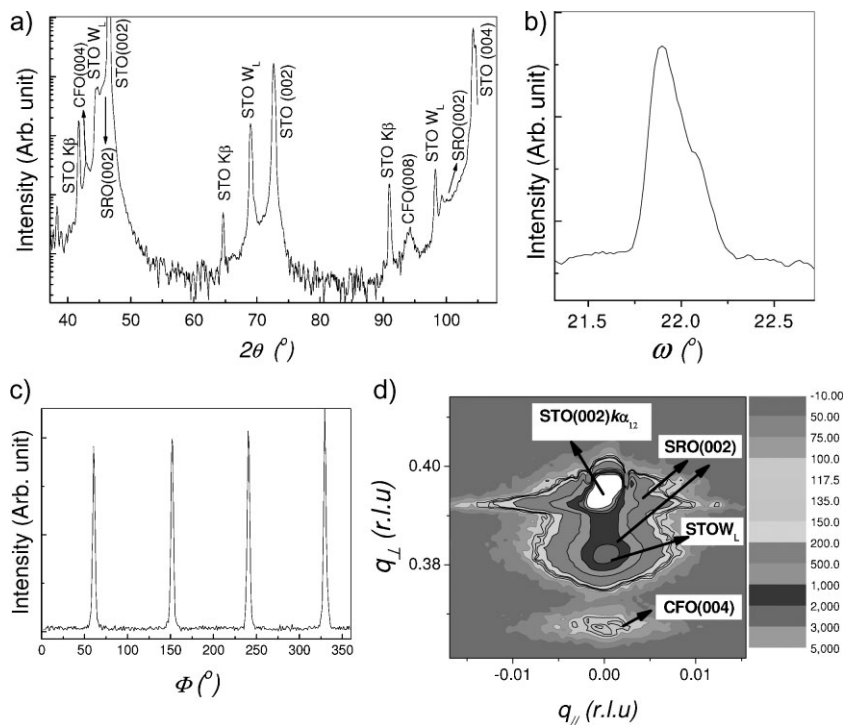


Figure 7. a) XRD diffraction pattern of an epitaxial CFO nanodot array (diameter: ~ 290 nm, height: ~ 40 nm) obtained at a high deposition temperature of 500°C and an oxygen pressure of 0.02 mbar. b) Rocking curve of the CFO (004) diffraction peak showing a narrow FWHM of 0.3° . c) Φ -scan of the CFO (110) peak indicating a cubic-on-cubic growth of CFO on SRO. d) Reciprocal space mapping along the STO (002) reflection further confirming the epitaxial growth of CFO.

perpendicular spin contributions), and the schematic diagrams for the corresponding MFM state images are also shown. Several different states can be observed within the same array (Fig. 8e), that is, bubble domain (i), reversed bubble domain (ii), decentered bubble domain (iii), stripe domain (iv), single-domain state (v), and two hemicylindrical domains (vi). The existence of similar bubble and stripe domains was previously reported in epitaxial Co dots^[28] where perpendicular anisotropy and demagnetization field play very critical roles. Due to the large demagnetization energy, a single domain in this system is unstable and tends to split into two or more domains. In spinel CFO dots, the mechanisms are very complicated because several major factors, for example, exchange energy, crystalline anisotropy, magnetoelastic anisotropy, and magnetostatic (demagnetization) energy, are competing with each other leading to a range of stable/metastable states, which will also be the subject of further investigations.^[29,30] The stability of the complex domain structures in CFO dots indicates that the demagnetization (magnetostatic energy) plays an essential role. Such domain splitting is more likely to occur in single crystalline rather than in polycrystalline dots, as the perpendicular anisotropy (e.g., crystalline and magnetoelastic anisotropies) is also important to maintain the out-of-plane magnetization.^[29] The spin state inside the array is not very uniform, probably due to defects and shape imperfections, and more homogenous states could be obtained by further improving the shape uniformity of the dots. By further adjusting the deposition and shape geometry parameters

we were able to achieve uniform single domains (Supporting Information, Fig. S1).

The observation of bubble and other complex domains in epitaxial spinel oxide nanodots are interesting both from fundamental research and application viewpoints. It paves the way to further investigate the micromagnetization inside nanostructures and control the spin states through strain and possible magnetoelectric effects. It also creates opportunities for device applications like memories, as bubble domains are rather stable against disturbance compared to single domains. Furthermore, the direct growth of epitaxial nanostructures is promising for designing more complicated dot array structures, for example, multilayer spin filters for either device applications or fundamental research.

3. Conclusions

Well-ordered CFO nanodot arrays were successfully fabricated by a combination of PLD and ultra-thin self-organized AAO masks. The dot size was varied from 35 to 300 nm and the interdot distance from 60 to 500 nm. These dots show slim magnetization hysteresis loops and a unique temperature-dependent magnetic behavior. MFM images indicate a cluster-like magnetic behavior from the dipole-dipole interaction between small dots (diameter ~ 60 nm) and more-or-less individual magnetic behavior for larger dots (diameter ~ 300 nm). Finally, by optimizing the deposition parameters, we were able to obtain epitaxial dot arrays, as confirmed by XRD Φ -scans and reciprocal space mappings. The epitaxial dots demonstrate complex multidomain structures such as bubble domains or stripe domains due to the large demagnetization inside the dots.

4. Experimental

Fabrication of Nanodot Arrays: The fabrication procedure is schematically illustrated in the flow chart of Figure 1a. A conducting layer of SRO was deposited on single-crystalline substrates of STO or MgO by PLD for the purpose of a better adhesion and control of the magnetic properties (i). Ultrathin AAO masks with self-ordered arrays of pores with various pore sizes and pitches were prepared by an anodizing technique as described elsewhere [21,22]. The ultrathin AAO mask was then transferred onto the substrate (ii). Subsequently the CFO was deposited through the mask by PLD in an ambient pressure from 10^{-5} bar to 0.05 mbar at elevated temperatures ranging from 200 to 550°C (iii). Finally, the AAO mask was mechanically removed to obtain extended arrays of CFO nanodots (iv).

Instruments: The crystal structure was characterized by XRD θ - 2θ scans using a Philips X'Pert MRD diffractometer with $\text{CuK}\alpha$ radiation. Magnetic properties were characterized by SQUID magnetometry and MFM (SPM, DI 5000) with a tip-height range of 50 – 100 nm. SEM images were obtained by a JEOL JSM-6300F microscope. TEM investigations were conducted by a Philips CM20T (Philips, Netherlands) at a voltage of 200 kV and a HRTEM JEOL 4010 (JEOL, Japan) at 400 kV. The samples for TEM were thinned using mechanical and ion-beam-based standard methods.

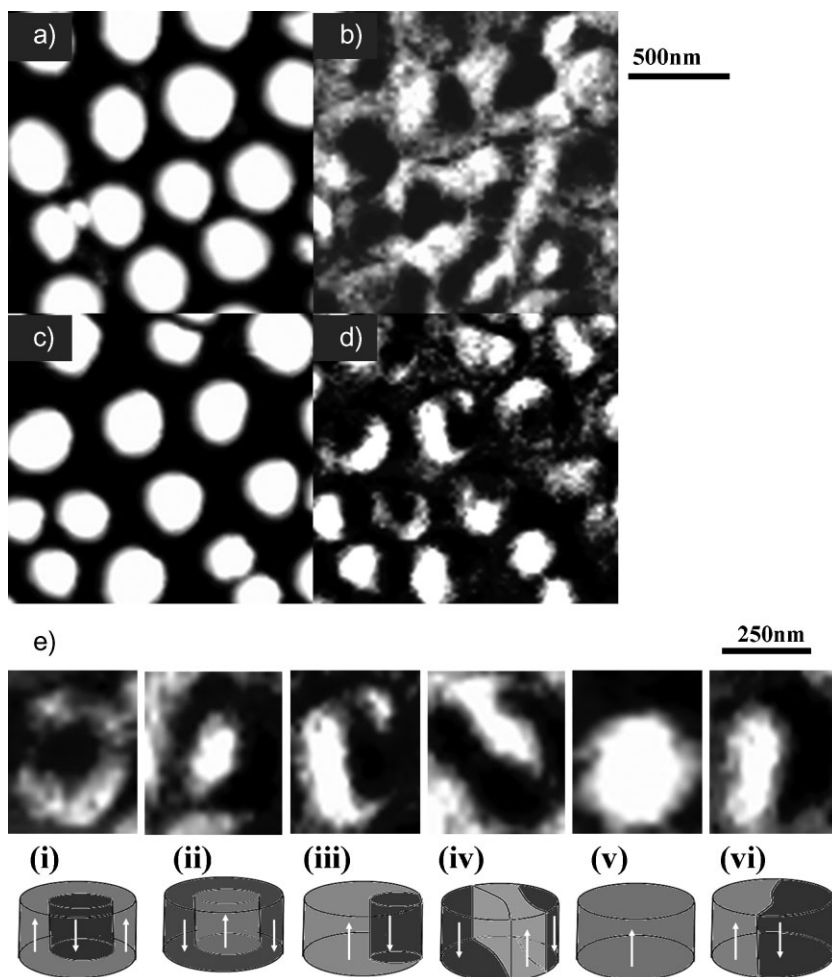


Figure 8. AFM topography images (a,c) and MFM micrographs (b,d) for epitaxial CFO dots (diameter: ~ 290 nm, height: ~ 80 nm) that are premagnetized by a field (H) perpendicular to the surface (a,b) and switched by a reversed magnetic field ($-H$) to investigate the switching of the magnetic states (c,d). Enlarged MFM images of various spin states that are picked up from (b) and (d) and their corresponding schematic spin configurations are shown in (e), in which a range of domain states are demonstrated: bubble domain (i), reversed bubble domain (ii), decentered bubble domain (iii), stripe domain (iv), single domain state (v), and hemicylindrical bidomain state (vi).

Acknowledgements

X.-S. G. acknowledges the Alexander von Humboldt Foundation for financial support. This work was partially supported by the German Science Foundation (DFG) via SFB 762. Professor D. H. Bao (Sun Yat-Sen University, Guangzhou, P.R. China), Mr. M. A. Schubert, and Dr. R. Hillebrand are acknowledged for technical support and most helpful discussions. Supporting Information is available online from Wiley InterScience or from the author.

Received: March 11, 2009

Published online: August 31, 2009

[1] G. Hu, J. H. Choi, C. B. Eom, V. G. Harris, Y. Suzuki, *Phys. Rev. B* **2000**, 62, R779.

- [2] W. Huang, J. Zhu, H. Z. Zeng, X. H. Wei, Y. Zhang, Y. R. Li, *Appl. Phys. Lett.* **2006**, 9, 262506.
- [3] A. Lisfi, C. M. Williams, L. T. Nguyen, J. C. Lodder, A. Coleman, H. Corcoran, A. Johnson, P. Chang, A. Kumar, W. Morgan, *Phys. Rev. B* **2007**, 76, 054405.
- [4] M. J. Carey, S. Maat, P. Rice, R. F. C. Farrow, R. F. Marks, A. Kellock, P. Nguyen, B. A. Gurney, *Appl. Phys. Lett.* **2007**, 81, 1044.
- [5] H. Zheng, J. Wang, S. E. Lofland, Z. Ma, L. Mohaddes-Ardabili, T. Zhao, L. Salamanca-Riba, S. R. Shinde, S. B. Ogale, F. Bai, D. Viehland, Y. Jia, D. G. Schlom, M. Wuttig, A. Roytburd, R. Ramesh, *Science* **2004**, 303, 661.
- [6] S. D. Bader, *Rev. Mod. Phys.* **2006**, 78, 1.
- [7] S. H. Sun, H. Zeng, D. B. Robinson, S. Raoux, P. M. Rice, S. X. Wang, G. X. Li, *J. Am. Chem. Soc.* **2004**, 126, 273.
- [8] K. Raj, R. Moskowitz, *J. Magn. Magn. Mater.* **1990**, 85, 233.
- [9] D. H. Kim, D. E. Nikles, D. T. Johnson, C. S. Brazel, *J. Magn. Magn. Mater.* **2008**, 320, 2390.
- [10] P. Oswald, O. Clement, C. Chambon, E. Schouman-Claeys, G. Frijia, *Magn. Reson. Imaging* **1997**, 15, 1025.
- [11] B. H. Liu, J. Ding, Z. L. Dong, C. B. Boothroy, J. H. Yin, J. B. Yi, *Phys. Rev. B* **2006**, 74, 184427.
- [12] G. B. Ji, S. L. Tang, B. L. Xu, B. X. Gu, Y. W. Du, *Chem. Phys. Lett.* **2003**, 379, 484.
- [13] A. K. Srivastava, S. Madhavi, T. J. White, R. V. Ramanujana, *J. Mater. Res.* **2007**, 22, 1250.
- [14] Y. D. Meng, D. R. Chen, X. L. Jiao, *Eur. J. Inorg. Chem.* **2008**, 2008, 4019.
- [15] Y. Li, Q. Zhang, A. V. Nurmikko, S. Sun, *Nano Lett.* **2005**, 5, 1689.
- [16] Z. T. Zhang, A. J. Rongdingone, J. X. Ma, J. Shen, S. Dai, *Adv. Mater.* **2005**, 17, 1415.
- [17] Z. X. Pan, N. Alem, T. Sun, V. P. Dravid, *Nano Lett.* **2006**, 6, 2344.
- [18] O. Ersen, S. Bégin, M. Houllé, J. Amadou, I. Janowska, J.-M. Grenèche, C. Crucifix, C. Pham-Huu, *Nano Lett.* **2008**, 8, 1033.
- [19] C. A. Ross, *Annu. Rev. Mater. Res.* **2001**, 31, 203.
- [20] J. I. Martin, J. Nogues, K. Liu, J. L. Vicent, I. K. Schuller, *J. Magn. Magn. Mater.* **2003**, 256, 449.
- [21] W. Lee, H. Han, A. Lotnyk, M. A. Schubert, S. Senz, M. Alexe, D. Hesse, S. Baik, U. Gösele, *Nat. Nanotechnol.* **2008**, 3, 402.
- [22] H. Masuda, K. Fukuda, *Science* **1995**, 268, 1466.
- [23] W. Lee, M. Alexe, K. Nielsch, U. Gösele, *Chem. Mater.* **2005**, 17, 3325.
- [24] S. K. Lee, D. Hesse, M. Alexe, W. Lee, K. Nielsch, U. Gösele, *J. Appl. Phys.* **2005**, 98, 124302.
- [25] W. Lee, R. Ji, U. Gösele, K. Nielsch, *Nat. Mater.* **2006**, 5, 741.
- [26] X. S. Gao, D. H. Bao, B. Birajdar, R. Mattheis, M. A. Schubert, M. Alexe, D. Hesse, *J. Phys. D: Appl. Phys.*, in press.
- [27] W. H. Wang, X. Ren, *J. Cryst. Growth* **2006**, 289, 605.
- [28] M. Hehn, K. Ounadjela, J.-P. Bucher, F. Rousseaux, D. Decanini, B. Bartenlian, C. Chappert, *Science* **1996**, 272, 1782.
- [29] G. Hrkac, S. Bance, A. Goncharov, T. Schrefl, D. Suess, *J. Phys. D: Appl. Phys.* **2007**, 40, 2695.
- [30] Q.-L. Ye, Y. Kozuka, H. Yoshikawa, K. Awaga, S. Bandow, S. Iijima, *Phys. Rev. B* **2007**, 75, 224404.